Engineering the Work Function of Buckled Boron α-Sheet by Lithium Adsorption: A First-Principles Investigation

Bing Zheng, Hai-tao Yu,* Ying Xie, and Yong-fu Lian*

School of Chemistry and Materials Science, Key Laboratory of Functional Inorganic Material Chemistry, Ministry of Education of the People's Republic of China, Heilongjiang University, Harbin 150080, P. R. China

S *Supporting Information*

ABSTRACT: First-principles density functional theory calculations were performed to study the effect of Li adsorption on the structural and electronic properties, particularly the work function, of boron α-sheet. The calculated binding energies indicated that boron α-sheet could be well stabilized by the adsorption of Li atoms. Furthermore, the work functions of Li-adsorbed boron α-sheets were observed to decrease drastically with increasing Li coverage. The work functions are lower than that of Mg and even, for some of them, lower than that of Ca, indicating a considerable potential application of Li-adsorbed boron α-sheets as field-emission and electrode materials. Based on the calculated geometric and electronic structures, we discuss in details some possible aspects affecting the work function. The Li coverage dependence of the work functions of Li-adsorbed boron α-sheets was further confirmed by electrostatic potential analyses. The relationship between the work function variation and the Fermi and vacuum energy level shifts was also discussed, and we observed that the variation of the work function is primarily associated with the shift of the Fermi energy level. It is the surface dipole formed by the interaction between adatoms and substrate that should be responsible for the observed variation of the work function, whereas the increasing negative charge and rumpling for boron α-sheet only play minor roles. Additionally, the effect of Li adatoms on the work function of boron α-sheet was confirmed to be much stronger than that of graphene or a graphene double layer.

KEYWORDS: buckled boron α-sheet, work function, binding energy, electronic structure, electrostatic potential, electronic population
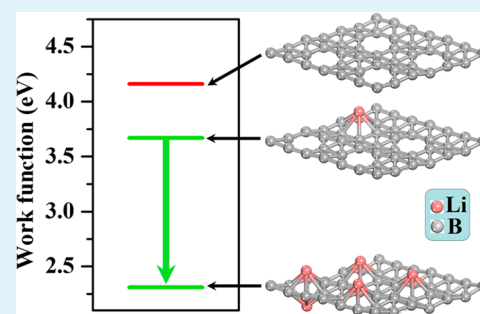
INTRODUCTION

Recently, low-dimensional nanomaterials, including C,[1−4] Si,[5] ZnO,[6] TiO$_2$,[7] B,[8−20] B$_x$C$_y$,[21] B$_x$N$_y$,[22] and B$_x$C$_y$N$_z$,[23] have received massive attention due to their structural characteristics and unique properties. Carbon, in particular, can form all three low-dimensional allotropes, including experimentally available zero-dimensional (0D) fullerenes,[1] one-dimensional (1D) carbon nanotubes (CNTs),[2] and two-dimensional (2D) graphene.[3] Graphene is a monatomic layer composed of sp^2-bonded carbon atoms arranged in a honeycomb-like structure. Its conically shaped valence and conduction bands touch each other in the reciprocal space of a 2D lattice, leading to a zero-gap semiconductor.[4] The gapless feature of graphene makes it very difficult to work with in some special fields, such as turning transport off when trying to mimic a conventional switch or transistor. Thus, a constant effort has been made to engineer its bandgap using different methods, such as size confinement (nanoribbons)[24] and chemical modification.[25] Motivated by the remarkable productive investigations of graphene, studies have paid increasing attention to some other 2D materials, such as BC,[21] BN,[22] BCN,[23] BNO,[26] graphane,[26,27] and graphene oxide.[26,27]

Boron and boron-based structures possess some significantly favorable properties, including excellent chemical stabilities, low densities (2.364 g/cm^3),[28] high melting points over 2300 °C

(approximately 1000 °C higher than silicon),[28] large bulk Young's moduli of 380−400 GPa,[28] hardness similar to that of diamond,[28] high thermal conductivities,[29] and high electric conductivities.[29] These structures are applicable in the fields of flexible electronics,[28] field-emission (FE) materials,[29] hydrogen storage media,[30−32] and lithium-ion batteries.[33] To date, a range of 0D hollow boron molecular structures have been experimentally and theoretically proposed,[34−38] and some experimental works regarding 1D nanoboron structures such as single- and multiwalled nanotubes (BNTs),[29,39] nanowires,[40] boron nanorods,[41] nanobelts,[42] and nanoribbons[43] have been reported. For 2D nanoboron structures, the graphene-like hexagonal sheet, buckled triangular sheet, α-sheet, β-sheet, and γ-sheet[8−12] have been predicted theoretically, and sheets constructed from hexagon holes and filled hexagon motifs (Figure 1), including α- and α$_1$-sheets are suggested to be the most stable.[12,13] However, because of their structural flexibility and competing energetic ordering, the exact ground state configuration still remains an open question. To determine the most stable 2D lattice configuration, many boron sheets (α-sheet, β-sheet, g$_{1/8}$-sheet, g$_{2/15}$-sheet, α$_1$-sheet, and β$_1$-sheet),
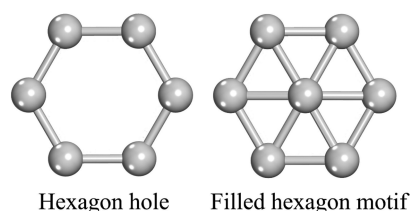
Hexagon hole   Filled hexagon motif

Figure 1. Structures of hexagon hole and filled hexagon motif.

which are based on hexagon holes and filled hexagon motifs, were systematically investigated using theoretical chemistry calculations.[14−18] Li and co-workers studied the electronic structure of boron α-sheet using the adaptive natural density partitioning (AdNDP) method.[19] These researchers concluded that the sheet could be stabilized when hexagon holes served as scavengers of extra electrons from filled hexagons. Such a chemical bonding model is helpful for our understanding of the chemical bonding in all-boron nanomaterials.

Recently, a highly stable quasiplanar boron cluster (B_{36}) bearing a central hexagonal hole was observed,[20] which could be extended to 2D boron sheets. This result provides direct evidence of the existence of monolayer boron sheet constructed from hexagon holes and filled hexagon motifs. In addition, other indirect evidence is available to support the existence of boron sheets.[12,13] The α-sheet and α_1-sheet, two types of models of stable boron sheets, can be viewed as being directly related to the synthesized BNTs. Similar to the relationship between CNTs and graphene, a single-walled boron nanotube (SWBNT) is considered to be formed by rolling up a boron monolayer sheet, and a multiwalled boron nanotube (MWBNT) is considered to be formed by rolling up a multilayered sheet. According to Wu et al., a bilayer α_1-sheet remains flat with an optimized interlayer distance of ~3.62 Å,[12] which is close to the experimental value of ~3.2 Å in the MWBNTs synthesized by Liu et al.[29] Furthermore, the work function of α-sheet is calculated to be 4.09 eV,[13] which is also in agreement with the experimental value of 4.02 eV for MWBNTs.[29]

It should be noted that BNTs have been shown to be highly conductive,[29] implying that boron sheets should be metallic, in line with many theoretical investigations.[13,15,16] However, Wu et al. proposed that the α-sheet is a semiconductor with an indirect band gap of 1.40 eV, while the α_1-, β_1-, $g_{1/8}$-, and $g_{2/15}$-sheets are metallic.[12] Therefore, it is necessary to perform further works to clarify the issue.

The work function is an important physical quantity for electrode materials, correlating with their maximum energy conversion efficiencies when used in light-emitting diodes (LEDs), organic light-emitting diodes (OLEDs), and organic solar cells (OSCs).[44] Recently, particular attention has been paid to engineering the work functions of some 2D materials, such as graphene,[44,45] reduced graphene oxide,[46] BN sheets,[47,48] and $C_x(BN)_y$ monolayers.[49] When 2D materials are employed as anode or cathode materials, their work functions are always to be adjusted for achieving a match in the energy level between the 2D materials and other active layers or substrate.[45] Additionally, the field emission performance of 2D materials can be dramatically improved with their work functions decreased. Thus, the modulation for the work functions of 2D materials on the atomic scale is crucial for maximizing device performances.

The work functions of some 2D materials were reported to be engineered using an external electric field,[50] chemical and metal dopings (or decorations),[44,45] substrate orientations,[51] and self-assembled monolayers or metal oxide layers.[52,53] Among these approaches, chemical and metal dopings were performed using n-type or p-type dopants.[44,45] Generally, the n-type doping was effective to reduce the work functions of 2D materials, while the p-type doping was effective to enhance the work functions of 2D materials. Moreover, a few feasible methods along with possible mechanisms for the engineering of the work function were proposed theoretically.[51,55,56]

Boron sheets are novel and promising 2D materials; the engineering of their work functions is essential for the design of nanoscale electric devices. Considering that the BNTs fabricated by Liu et al. possess good field-emission properties[29] and that the work function of plane boron α-sheet (PBST) is as high as 4.02 eV, the boron α-sheet with its work function reduced to some extent should be useful for particular applications in field emitters, LEDs, OLEDs, OSCs, and other devices. Unfortunately, to the best of our knowledge, there are still no reports on the engineering of the work function of boron sheets. It is well-known that alkali-metals can be used as n-type dopants to reduce the work functions of many other materials.[57] For example, the work function of a few-layer graphene could be reduced from 4.25 eV (graphene) to 3.8, 3.7, 3.5, and 3.4 eV, which is comparable with Mg (3.68 eV), by doping with Li_2CO_3, K_2CO_3, Rb_2CO_3, and Cs_2CO_3, respectively.[44] A theoretical study also concluded that the work function of a graphene double layer could be radically reduced by alkaline atom (K or Li) intercalation.[55] Thus, it is reasonable to deduce that the work function of boron α-sheet can be reduced by doping with alkali-metal atoms. Unlike graphene, which contains robust traditional sp^2 hybridization bonding features, boron α-sheet possesses fascinating multicentered bonds. In particular, its hexagon holes can serve as scavengers of extra electrons from its filled hexagons[19] and can be viewed as "electron deficiency regions". The bonds in the "electron deficiency regions" should be somewhat weaker than those in the hexagon holes of graphene, and then, the adsorption of alkali-metal atoms on boron α-sheet is expected to occur more easily than on graphene.[58] Therefore, it is reasonable to estimate that the Li-decorated boron α-sheet with a Li atom adsorbed on the site above the center of an empty boron hexagon is more stable than Li_n/graphene.[59] It is expected that the work functions of Li-coated planar boron α-sheets are tunable by their topologies and Li contents, which makes them an ideal host material for electronic devices.

Herein, we report a first-principles investigation of the work functions of Li-absorbed boron α-sheets with the aim to provide a potential experimental method of decreasing the work function of boron α-sheet and to contribute to a better understanding of the interaction between Li adatoms and boron α-sheet in engineering the work function of boron α-sheet. Our main concerns are (i) the stabilities of Li-adsorbed boron α-sheet compounds, (ii) whether the work function changes with Li concentrations and configurations, and (iii) possible mechanisms for work function modification by Li adatoms.

■ COMPUTATIONAL METHODS

In this study, all the calculations were performed within the density functional theory (DFT) framework by employing the $Dmol^3$ package except the electron density difference. The
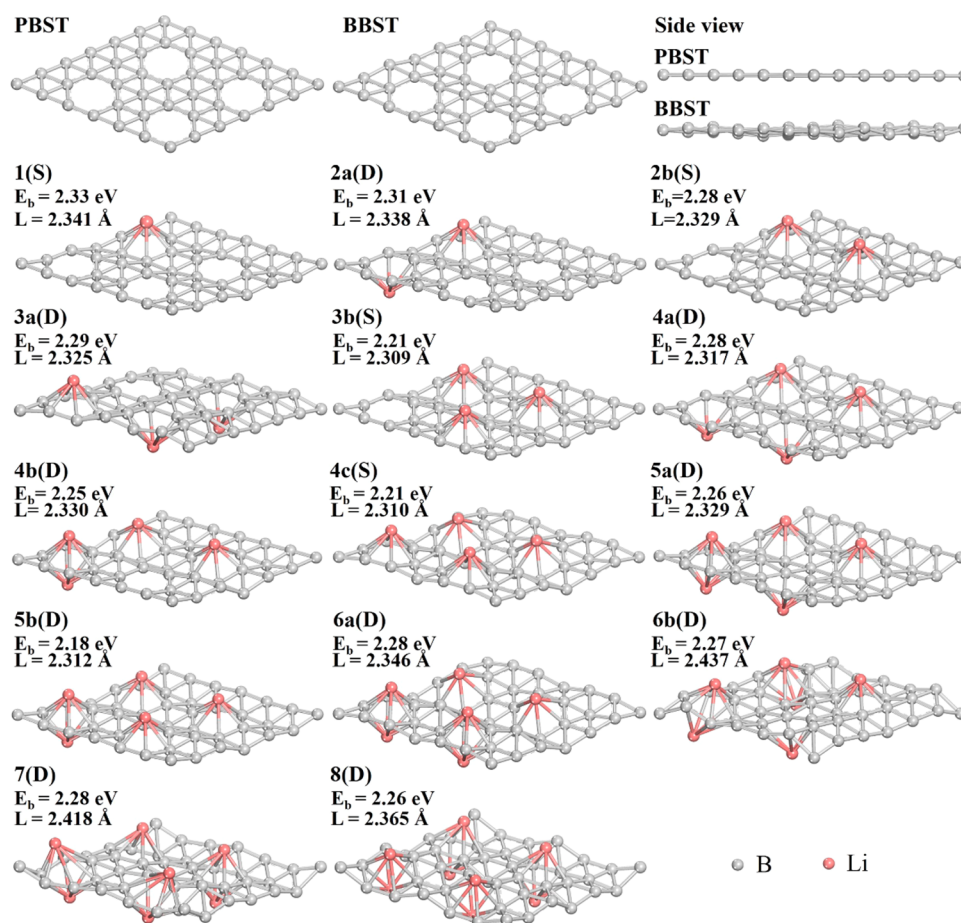
Figure 2. Optimized structures of PBST, BBST, and Li_n/BBST models. E_b and L are the binding energies and Li−B average bond lengths of Li_n/BBST systems, respectively.

exchange-correlation energy was treated using the Perdew−Wang (PW91) functional in the generalized gradient approximation (GGA) form[60] because PW91 could describe well the most prominent interactions in alkali-metal doped systems,[61] that is, chemical bonding and electrostatic interactions. The basis functions were described by a double numerical plus polarized (DNP) basis set, and the global orbital cutoff was preliminarily tested and set to 5.1 Å. For the core treatment, all the electrons were explicitly included and unrestricted spin was also considered. The Monkhorst−Pack scheme was used to sample the Brillouin zone (BZ), and a mesh of $6 \times 6 \times 1$ k-points sampling was employed in the calculations. For each supercell, a vacuum region of 16 Å along the surface normal was set to ensure the cancellation of spurious interactions between periodic images. During geometry optimizations, the structures were fully relaxed until the residual forces were smaller than 2×10^{-3} hartree/Å, the changes in energy were reduced to less than 10^{-5} hartree, and atomic displacements were smaller than 5×10^{-3} Å. The calculations of the frequencies, densities of states (DOSs), electron densities, electrostatic potentials, and electronic populations were performed for further analysis of electronic structures and work functions. To obtain the minimum energy pathway (MEP), all of the given transition states in this work were located using the complete linear/quadratic synchronous transit (LST/QST)[62,63] and nudged elastic band (NEB)[64] methods.

In the calculations of electron density differences, performed using ultrasoft pseudopotentials generated from the "on-the-fly" method implemented within the CASTEP, the GGA with PW91 exchange and correlation functional[60] was used, along with a plane-wave cutoff energy of 400 eV and the sampling over BZ of a $(6 \times 6 \times 1)$ Monkhorst−Pack mesh.

RESULTS AND DISCUSSION

Models and Configurations. We first optimized the geometry of boron α-sheet. Previous studies revealed that there are two possible structures of boron α-sheet, involving PBST and buckled boron α-sheet (BBST), as described in Figure 2. According to PBE and PBE0,[12] the phonon frequencies in the calculated phonon spectrum of PBST are negative. The eigenvector of the negative frequency mode manifests an out-of-plane bending vibration. In contrast, the BBST does not exhibit any negative phonon frequency and has a greater binding energy than PBST. The PW91 results in this study are in good accordance with the above PBE and PBE0 calculations. Therefore, the BBST structure should be more rational than the PBST model, and it is reasonable for us to employ BBST as the substrate in this study.

Next, we turn to test the adsorption sites of Li atoms on BBST. The optimized results indicate that Li adsorption on the site above the center of an empty boron hexagon (i.e., the middle hollow site (MHS)) is energetically more favorable than on any other positions. This result coincides with the adsorption sites of Li atoms on both PBST and boron β-
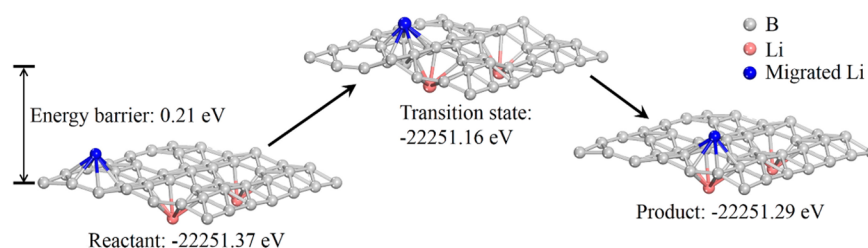
Figure 3. Schematic diagram of Li-shift pathway in Li$_3$/BBST.

sheet reported previously.[59,65] Indeed, such an adsorption behavior has also been observed in other systems, such as graphene,[58] carbon nanotubes,[66] fullerenes,[66] boron nanotubes,[31] and boron fullerenes.[31] We herein constructed original adsorption models (Li$_n$/BBST) by adding Li atoms above the MHSs of boron hexagons and performed further geometry optimizations. Single- and double-side-adsorbed models were achieved in line with the Li atoms being adsorbed on one side or two sides of BBST. These geometries are called as nX(S) or nX(D), respectively, in which n, ranging from 1 to 8, corresponds to the number of Li atoms in Li$_n$/BBST, X is the sequence number (a, b, c, ...) of different Li$_n$/BBST models with the same n, and S and D represent single- and double-side-adsorbed models, respectively.

In this investigation, a 2×2 supercell containing thirty-two boron atoms, four hexagon holes, and eight MHSs was adopted. The Li adsorption concentration was ascribed by the hole coverage (HC), that is, the number of adsorbed Li atoms on BBST divided by eight (the total number of MHSs in a 2×2 supercell). It should be noted that the existence of different configurations is possible even under the same adsorption concentration due to the structural distortions of BBST and the varying absorption sites of Li atoms.

Nonetheless, if Li adatoms can shift easily among different MHSs, the thermodynamic probabilities of the configurations with lower binding energy are relatively low. To evaluate possible diffusions of Li atoms on BBST, we calculated Li-shift energy barriers. The computed results, presented in Figures S1(a) and S1(b) in the Supporting Information, indicate that in the Li/BBST system the barriers for Li atom diffusions from the adsorbed site to two adjacent MHSs are 0.30 and 0.37 eV. Another computed result yielded a diffusion barrier of only 0.21 eV for Li$_3$/BBST, as shown in Figure 3. The above results are comparable to the theoretical barrier (0.45 eV, PW91 functional) for Li adatom diffusion on PBST given by Er et al.[59] In addition, it has been reported that the theoretical diffusion barriers (PBE functional) of Li atoms on graphene are 0.311 and 0.337 eV via bridge and top site transition states, respectively.[58] Moreover, for most metal adatoms, the diffusion within the *fcc* region of the graphene moiré superstructure formed on Ru (0001) is very facile.[67] It appears that the diffusion of Li atoms on BBST is effortless, and the Li$_n$/BBST systems with lower binding energy should thus be kinetically less stable.

It has been demonstrated that the Li atoms attached on graphene tend to cluster as the number of Li atoms increases.[68] There is an open question whether the attached Li atoms on BBST reported here prefer to remain isolated or aggregate with the increase of HC. To better understand the query, we placed several Li atoms on a boron hexagonal hole to construct computational models and performed further optimizations. As shown in Figure 2, after relaxing the constructed models, we

observed that the optimizations yield adsorbed geometries with no more than one Li atom on or below each MHS, and no clustering was observed. According to Er et al.,[59] a substantial effective charge carried by Li atoms is responsible for the configuration of Li adatoms on boron α-sheet.

Consequently, in this study, the configurations of Li$_n$/BBST with both higher binding energies and Li-single-layer were selected, and 14 structures with their optimized configurations shown in Figure 2 were investigated.

It should be noted that after adsorption the BBST substrate possesses a larger rumpling than the pristine BBST, and the adsorption sites of Li atoms in the configurations of **4b(D)**, **4c(S)**, **5a(D)**, **6a(D)**, **6b(D)**, **7(D)**, and **8(D)** obviously deviate from the corresponding MHSs. To estimate the average deformation of BBST after adsorption, we defined the average rumpling ($\bar{R}$) based on the calculated rumpling (R) along the z axis, which can be expressed as

$$\bar{R} = \frac{1}{32} \left[\sum_{m=1}^{32} |z_{m(\mathrm{Li}_n/\mathrm{BBST})} - z_{m(\mathrm{BBST})}| \right] \tag{1}$$

where $z_{m(\mathrm{Li}_n/\mathrm{BBST})}$ and $z_{m(\mathrm{BBST})}$ are the z coordinates of the boron atoms with a serial number of m in Li$_n$/BBST and BBST, respectively. In Figure S2 in the Supporting Information, the calculated R and $\bar{R}$ of the Li$_n$/BBST systems as a function of HC are shown. It can be observed that both R and $\bar{R}$ become increasingly larger with an increase in the number of Li adatoms, especially those structures with larger Li atom deviation from MHSs.

Binding Energies. The binding energy (E_b) was used to evaluate the interaction strength between the Li atoms and BBST:

$$E_b = \frac{1}{n} [E(\mathrm{BBST}) + nE(\mathrm{Li}) - E(\mathrm{Li}_n/\mathrm{BBST})] \tag{2}$$

where $E(\mathrm{BBST})$, $E(\mathrm{Li})$, and $E(\mathrm{Li}_n/\mathrm{BBST})$ represent the energies of the pristine BBST, a free Li atom, and Li$_n$/BBST, respectively. Figure 4 shows the calculated binding energies of Li$_n$/BBST systems using formula 2 as a function of the value of HC. It is observed that among all the optimized models, the binding energies (2.18–2.33 eV) are larger than either that reported previously (1.79 eV per Li atom) or that calculated in this work (1.65 eV, $I_{m\bar{3}m}$) in Li bulk. Hence, a clustering of the adsorbed Li atoms on BBST should be thermodynamically less favorable. This result is in good agreement with our aforementioned results (Figure 2 and Supporting Information Figure S1). Moreover, it is also observed that under the same Li adsorption concentration ($n = 2, 3, 4$), the single-side-adsorbed structure possesses lower binding energy than the corresponding double-side-adsorbed structure(s). Additionally, the fitted trendline in Figure 4 was generated from the structures with the highest binding energy for each HC. It is obvious that the
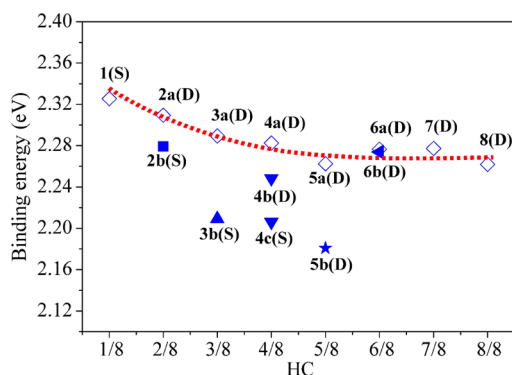
Figure 4. Binding energies of Li$_n$/BBST systems as a function of HC. The fitted trendline in red was generated from the structures possessing the maximum binding energy under the same HC.

binding energy gradually decreases and tends to converge as the value of HC increases, exhibiting a similar phenomenon in the Li/graphene systems.[58]

Generally, both BBST and Li adatoms can affect the binding energy change of Li$_n$/BBST with increasing HC. Using the calculated configuration geometries, we separated the two parts and performed single-point calculations with isolated BBST and Li adatoms as individual models. The calculated results are listed in Table S1 in the Supporting Information. In this table, the relative torsion energies (ΔE_{BBST}) of BBSTs in different Li$_n$/BBST models are computed by taking the BBST substrate of **1(S)** as a reference, and the cohesive energies (E_{coh}) of Li$_n$ clusters are computed using the expression

$$E_{coh} = \left(\frac{1}{n}\right)\left[E_{Li_n} - nE(Li)\right] \tag{3}$$

where E_{Li_n} and E_{Li} correspond to the single-point energy of the Li cluster in Li$_n$/BBST and the energy of a free Li atom, respectively, and n represents the number of adatoms. From the table, we can find that the BBST torsion energies exhibit a gradually increasing tendency with increasing HC. In contrast, the cohesive energies of the Li clusters exhibit the complete opposite tendency. Because the binding energies of Li$_n$/BBST are generally decreasing with increasing HC, we believe that such a decrease is dominated by the cohesive energies of Li clusters other than the torsion of BBST.

The Li$_n$/graphene system was widely regarded as a considerably potential material for hydrogen storage[69] and battery applications.[70] In Supporting Information Figure S4, the calculated Li$_n$/graphene configurations along with binding energies and average Li−C bond lengths are shown. It can be observed that the calculated binding energies of Li$_n$/graphene systems range from 0.97 to 1.38 eV, which are significantly lower than those of Li$_n$/BBST systems (2.18−2.33 eV). Furthermore, the binding energies of Li$_n$/graphene systems are even lower than the cohesive energy of the Li bulk (1.65 eV), indicating an unfavorable thermodynamic interaction between Li and graphene. This result is consistent with those reported previously.[58,59]

The poor thermodynamic stabilities of Li$_n$/graphene systems might be attributed to the perfect out-of-plane delocalized π bond of graphene, which is hard to be destroyed in forming new Li−C bonds. In sharp contrast, the formation of π bonds between Li atoms and BBST by $p-p$ interaction requires much lower energy (see the next section).

Electronic Structures. The Bader and Mulliken charges, total densities of states (TDOSs), partial densities of states (PDOSs), and electron density differences of Li$_n$/BBST systems were calculated to reveal the electronic properties of Li$_n$/BBST systems.

In Figure 5a, the average Bader and Mulliken charges of Li atoms in Li$_n$/BBST are shown. It can be seen that the average
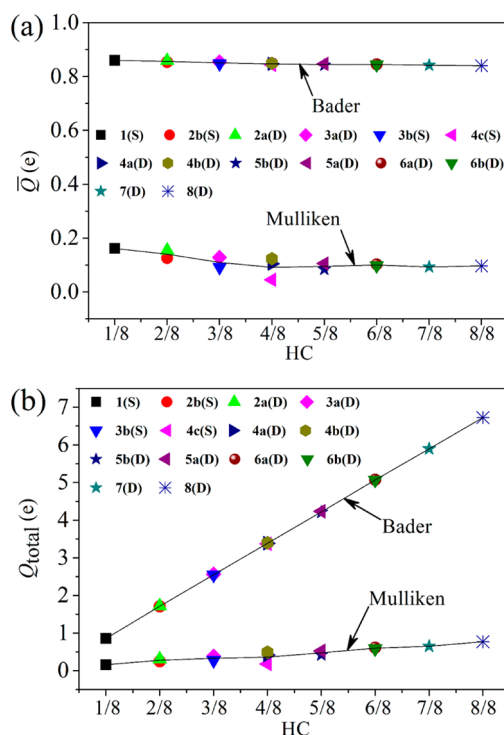
Figure 5. (a) Average Bader and Mulliken charges ($\overline{Q}$) and (b) total Bader and Mulliken charges (Q_{total}) of Li atoms in Li$_n$/BBST systems.

Bader and Mulliken charges reduce very slowly with increasing HC. Clearly, the average charges of Li atoms exhibit a similar HC dependence to the binding energy between Li atoms and BBST (see Figure 4). It should be noted that the average Mulliken charges vary from 0.05 e to 0.16 e, while the average Bader charges vary only between 0.84 e and 0.86 e. It is surprising that the average Bader charges are larger than the average Mulliken charges. The calculated Bader charges in this study are nearly the same as in the reported Li-adsorbed BST system ($\sim$0.8 e for the Li atom).[59] Similarly, the Bader charge of the Li atom on the defect-free graphene is $\sim$0.9 e.[71] These available data indicates that the Mulliken population analysis seems to underestimate the charges of Li adatoms. Thus, we would like to use the Bader population analysis in this study. In spite of this, we provide the two types of charges in next discussion for comparing their possible difference in electron transfer.

Figure 5b provides the computed total Bader and Mulliken charges (Q_{total}) of Li adatoms in Li$_n$/BBST. Generally, the change of Q_{total} of Li adatoms relates to the rumpling of BBST and the concentration of Li adatoms. The former would reduce the electron transfer from Li atoms to BBST, while the latter would enhance it. As shown in Figure 5b, Q_{total} increases linearly with increasing HC. Obviously, the raise of Li adatom number should be responsible for the increase in Q_{total}. Thus, the uptrend of Q_{total} for Li adatoms with increasing HC is not
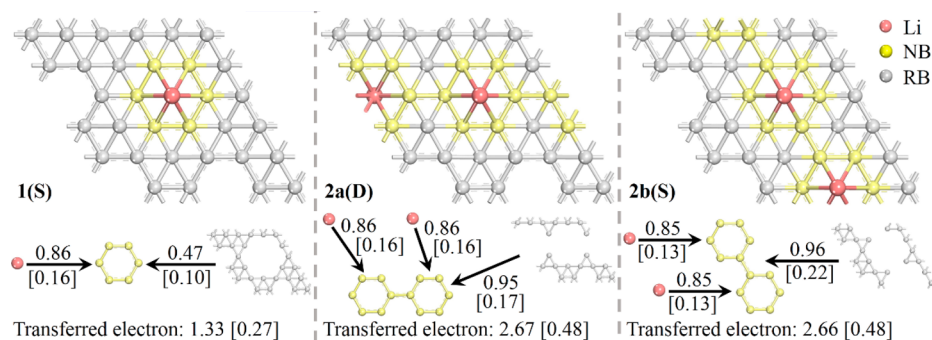
**Figure 6.** Computed electron transfers (*e*) in **1(S)**, **2a(D)**, and **2b(S)** from Bader and Mulliken (in square brackets) population analyses.

due to the increase of the rumpling of BBST but due to the increase of the number of Li adatoms.

To further explore the nature of electron transfer, we chose three representative systems, **1(S)**, **2a(D)**, and **2b(S)**, to calculate their detailed electron transfer number. In Figure 6, the calculated results are presented, in which the neighboring borons (NBs) represent the hexagonal boron atoms that are adjacent to Li atoms, and the remote borons (RBs) correspond to the boron atoms other than NBs. Based on the Bader charge analysis, the Li atom and RBs in **1(S)** transfer 0.86 *e* and 0.47 *e* to NBs, respectively. This result is in good agreement with the accepted total electrons of 1.33 *e* by NBs. The Mulliken population gives a similar trend. This finding indicates that in **1(S)**, Li and RBs are electron donors, and NBs are electron acceptors. A similar electron transfer behavior is also observed in **2a(S)** and **2b(D)**. Therefore, it is conjectured that Li atoms and RBs as electron donors and NBs as electron acceptors are universal in the investigated Li_n/BBST systems.

The TDOSs and PDOSs of Li_n/BBST systems were also calculated to further understand their electronic structures. As a representative example, the calculated data of **1(S)** were plotted in Figure 7, in which part a depicts the normalized TDOSs of Li and B atoms, and part b gives the normalized PDOSs of *s* and *p* orbitals of Li and B atoms. The inset in Figure 7b is the enlarged PDOSs of Li atoms after adsorption in the range of −16 to 2 eV. Figure 7a shows that the 2*s* orbital of the Li atom loses 0.15 *e* after adsorption based on the integrated peak area, which is in good agreement with the aforementioned electron transfer of 0.16 *e* from Li to BBST. In addition, there is no obvious difference between the TDOSs of the adsorbed BBST and the bare BBST, while the former shows an apparent feature of delocalization. Furthermore, the calculated TDOSs of BBST indicate that the peak area of the region filled with electrons (the region with energies less than the Fermi level) increases after adsorption. Thus, the BBST is an electron acceptor, suggesting a bonding interaction between BBST and the Li atom. Similarly, for NBs and RBs, the TDOS changes in the Li adsorption process are very slight, and the analysis of peak areas of the regions filled with electrons suggests that NBs and RBs are electron acceptors and donors, respectively. The conclusion coincides well with the analysis results in the previous section, that is, the electron transfer proceeds from Li and RBs to NBs.

The PDOS displayed in Figure 7b and the inset in Figure 7b reveal that the states at the Fermi energy level are mainly composed of the *p* orbitals of Li and B atoms, indicating that the bonding between Li and BBST corresponds to a *p*−*p* interaction. The hypothesized bonding process is as follows: the attached Li atom first donates its *s* electron to BBST (mainly NBs), leading to the *p* orbitals of B atoms being
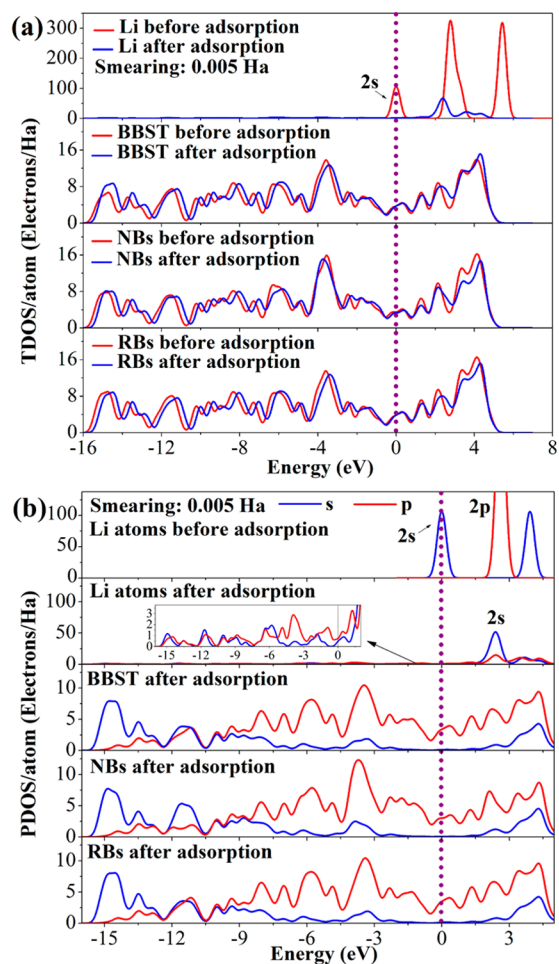
Figure 7. (a) TDOSs of Li and B atoms and (b) PDOSs of *s* and *p* orbitals of Li and B atoms for **1(S)**.

partially filled. Meanwhile, the empty *p* orbitals of Li atom split (Figure 7b) under the effect of the ligand field generated by BBST, and furthermore, the BBST donates some electrons back to the low-lying Li *p* orbitals, resulting in a strong hybridization between B 2*p* and Li 2*p* orbitals. Such an electron back-donation bonding mechanism can also be observed for Li binding onto zigzag BNTs,[30] B_{80} fullerene,[32] and other boron sheets.[65]

Figure 8 depicts the electron density difference with an isovalue of 0.47962 e/A^3 for Li_n/BBST systems ((**1(S)** and **5b(D)** as representing examples herein). In Li_n/BBST, the electron density in α regions above Li adatoms decreases, and
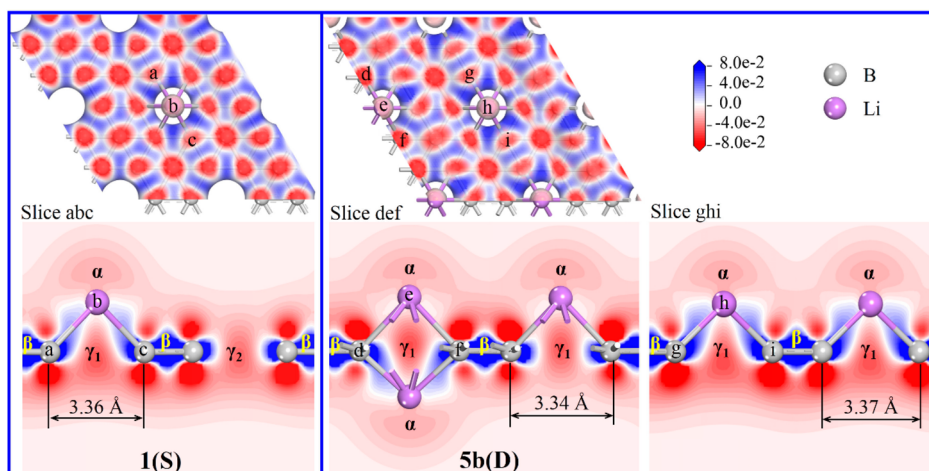
Figure 8. Electron density difference diagrams with an isovalue of 0.47962 e/A^3 for (**1(S)** and **5b(D)**). The density marked in blue corresponds to the region containing excess electrons, while the red areas represent electron-loss regions.

the regions between Li and B accept some electrons, indicating an obvious electron transfer from Li to BBST and a bonding interaction between Li and B atoms. Additionally, the fact that the β regions between two adjacent boron atoms accept some electrons suggests the existence of strong interactions forming the BBST skeleton. Another interesting finding is that the electron density in hexagonal holes (γ_1 and γ_2 regions) decreases relative to isolated atoms. Thus, no apparent interactions exist among the opposite boron atoms composing hexagonal holes. The results agree well with the pioneering study on the bonding nature of boron sheets by Galeev.[19]

Work Function. The work function is defined as the minimum energy required to remove an electron from a solid to a point immediately outside the solid surface or the energy needed to move an electron from the Fermi energy level into a vacuum. According to the latter, the work function (ϕ) can be formulated as

$$\phi = E_{vac,A} - E_{F,A} \tag{4}$$

where $E_{vac,A}$ and $E_{F,A}$ are the vacuum and Fermi levels of the system A, respectively.

Can the work function of BBST be engineered by tuning either the concentration of Li adatoms or the configurations of Li$_n$/BBST as we expected? In Figure 9, the calculated work
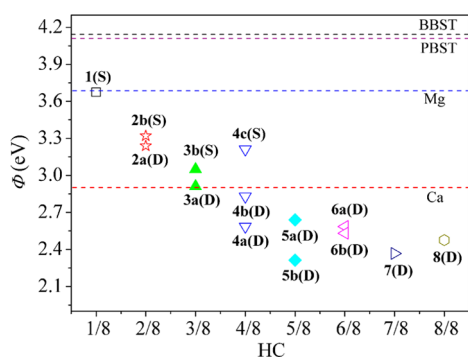
Figure 9. Work functions of Li$_n$/BBST systems. The blue and red horizontal lines correspond to the work functions of Mg and Ca, respectively, while the black and violet horizontal lines represent the work functions of BBST and PBST, respectively. The work functions were obtained by subtracting the Fermi level from the vacuum level.

functions of Li$_n$/BBST systems as a function of HC are shown. The work function of PBST predicted by PW91 is 4.11 eV, which is in good agreement with available theoretical (PBE, 4.09 eV)[13] and experimental data (4.02 eV).[29] It can also be observed that the work function decreases drastically from 3.67 eV (**1(S)**) to 2.31 eV (**5b(D)**) with increasing HC. Inspiringly, the case of the lowest work function (2.31 eV, **5b(D)**) shows a 44.5% decrease (1.85 eV) compared with the pristine BBST (4.16 eV) and 37.2% and 20.3% decreases relative to the frequently used electrode materials in electric devices, Mg (3.68 eV) and Ca (2.90 eV), respectively.[55] More importantly, the work functions of all the investigated Li$_n$/BBST systems are lower than Mg, and those with higher HC (**4a(D)**, **4b(D)**, **5a(D)**, **5b(D)**, **6a(D)**, **6b(D)**, **7(D)**, and **8(D)**) are even lower than Ca. Moreover, the work functions of the single-side-adsorbed structures are obviously higher than those of the double-side-adsorbed ones under the same HC. Additionally, the extent of reduction in the work function of Li$_n$/BBST systems is also larger than that in graphene bilayer materials with intercalated Li and K.[55] The dependence of the work function of BBST on the concentrations of Li adatoms and the configurations of Li$_n$/BBST implies that the work function of BBST can be effectively engineered by Li adsorption; furthermore, the work function would be accurately determined if the HC and configurations of Li$_n$/BBST can be availably adjusted in experiments.

Essentially, the work function is closely related to the electrostatic potential, and these parameters possess identical changing trends. Because the Li$_n$/BBST systems can be viewed as quasiplanar structures, we can evaluate the electrostatic potentials by comparing the same planes in different models. Figure 10 illustrates the slices of the electrostatic potential maps of BBST, **1(S)**, **3a(D)**, and **5b(D)**. The density marked in blue corresponds to the region that displays negative electrostatic potential, while that marked in red indicates a positive electrostatic potential. Every slice is determined by three points, each of which is located at almost the same position in the four configurations; see Figure S5 in the Supporting Information. From Figure 10, we know that the blue region grows rapidly from BBST to **1(S)**, **3a(D)**, and **5b(D)**, indicating an ascending negative electrostatic potential with increasing Li adatoms. This finding is in good accordance with the downtrend of the work function, as observed in Figure 9.
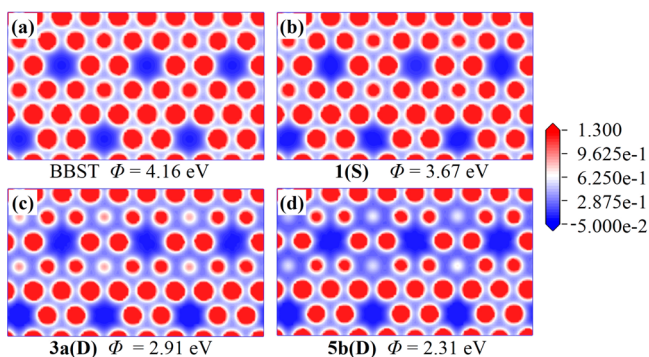
Figure 10. Slices of electrostatic potential maps for (a) BBST, (b) **1(S)**, (c) **3a(D)**, and (d) **5b(D)**. The density marked in blue corresponds to the regions that display negative electrostatic potential, while that marked in red indicates positive electrostatic potential. Every slice is determined by three points, each of which is located at almost the same position in the four configurations.

Therefore, Figure 10 further confirms the change of the work functions for Li_n/BBST systems as a function of HC. Because the work function is determined by E_F and E_{vac} (eq 4), an examination of HC and the structure dependences of the two terms can provide not only a dominant effect on the work function change but also a better understanding of the nature of the work function for such systems.

Figure 11a shows the Fermi and vacuum levels of the 14 configurations investigated as a function of the HC of lithium atoms. It can be observed from Figure 11a that E_F increases rapidly with increasing HC, and the configuration **5b(D)** possesses a maximum of −3.35 eV, which represents a 1.48 eV increase compared with BBST (−4.83 eV). However, the E_{vac}
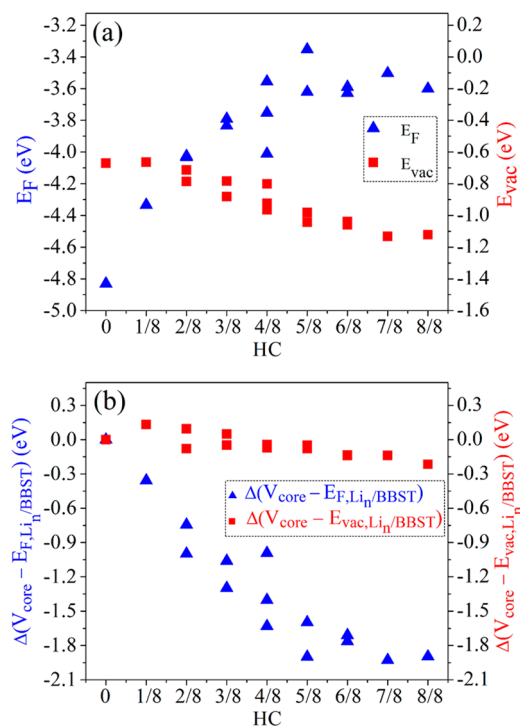
Figure 11. (a) Fermi and vacuum levels and (b) the relative offsets $\Delta(V_{core} - E_{vac,Li_n/BBST})$ and $\Delta(V_{core} - E_{F,Li_n/BBST})$ as a function of HC for Li_n/BBST systems. The y-axes of the left and right sides in the two figures are of uniform scale.

of Li_n/BBST decreases slowly with increasing HC, and the configuration **7(D)** has the lowest E_{vac} of −1.13 eV with a decrease of only 0.46 eV relative to BBST (−0.67 eV). It is unambiguous that the changes in HC and configuration exert a more significant effect on the Fermi level but an inconsiderable effect on the vacuum energy level. Thus, we conclude that the Fermi level plays a crucial role in determining the work functions of Li-adsorbed BBST systems and the vacuum energy level has a very slight effect.

To further evaluate the effects of Fermi and vacuum levels on work function, the work function expression (eq 4) was rewritten by inserting the average electrostatic potential energy at ionic cores (V_{core}),[54,72] that is,

$$\phi = (V_{core} - E_{F,Li_n/BBST}) - (V_{core} - E_{vac,Li_n/BBST}) \tag{5}$$

where n ranges from 0 to 8, and the offsets $(V_{core} - E_{F,Li_n/BBST})$ and $(V_{core} - E_{vac,Li_n/BBST})$ are the potentials relative to the Fermi and vacuum levels of Li_n/BBST, respectively. Using the bare BBST as a reference system, the two relative offsets can be written as

$$\Delta(V_{core} - E_{F,Li_n/BBST})$$
$$= (V_{core,Li_n/BBST} - E_{F,Li_n/BBST}) - (V_{core,BBST} - E_{F,BBST}) \tag{6}$$

and

$$\Delta(V_{core} - E_{vac,Li_n/BBST})$$
$$= (V_{core,Li_n/BBST} - E_{vac,Li_n/BBST})$$
$$- (V_{core,BBST} - E_{vac,BBST}) \tag{7}$$

where n ranges from 1 to 8. The calculated data based on formulas 6 and 7 are depicted in Figure 11b. The relative offset $\Delta(V_{core} - E_{vac,Li_n/BBST})$ in eq 7 varies from −0.22 to 0.13 eV with ascending HC, while the relative offset $\Delta(V_{core} - E_{F,Li_n/BBST})$ in eq 6 reduces significantly from −0.36 to −1.93 eV with ascending HC. It is apparent that the variation range of the former is smaller than that of the latter. Thus, the shift of the Fermi energy in Li_n/BBST is the dominant cause leading to the reduction in the work function; that is, the change of the electrostatic potential contributed to the ionic cores by valence electrons only plays a minor role in contributing to the change in the work function.

Now, we turn to exploring the possible factors affecting the work function of BBST after adsorption by Li atoms. Generally, two aspects are considered as the main factors in engineering the work function of a material by surface decoration. One is the extra electrostatic field aroused by the molecular dipoles between adsorbed species and the substrate; the other is the net charge change in the substrate via charge redistributions induced by the bonding interaction between adatoms and the substrate.[73−75] Additionally, the deviation from the pristine BBST geometry might also contribute to the work function to a lesser extent. To verify the effect of the three possible aspects on the work function, we performed some additional calculations. First, we removed all the Li atoms from each of the located Li_n/BBST geometries, and the remaining boron atoms compose a new model, which was called BBST′. Then, the BBST′ along with BBST′(−1) and BBST′(−2), that is, BBST′ with charges of −1 and −2, respectively, was used to

perform further single-point calculations to obtain their work functions. The calculated results are shown in Figure 12, from
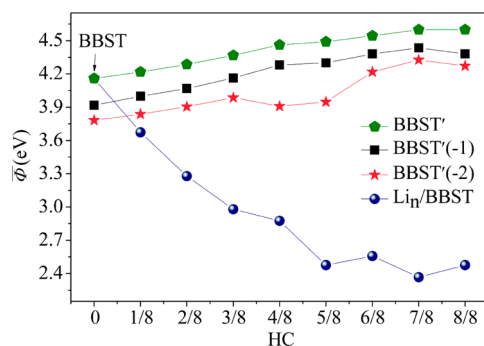
Figure 12. Average work functions of BBST′, BBST′(−1), BBST′(−2), and Li_n/BBST systems. The average work function is the average value of the work functions of different configurations under the same HC.

which one can know that the average work functions of BBST′, BBST′(−1), and BBST′(−2) increase with increasing HC. The aforementioned discussion states that the rumplings of BBST substrates increase with increasing HC, and thus, for BBST′, BBST′(−1), and BBST′(−2), the enlargement of BBST rumpling can lead to an ascending work function. Thus, the enlargement of BBST rumpling is not the factor resulting in the work function decrease of Li_n/BBST systems with increasing HC.

Moreover, the average work functions of BBST′, BBST′(−1), and BBST′(−2) under the same HC exhibit a downtrend trend as the negative charge increases. However, the reduction extent is somewhat smaller than that originating from Li adsorption. Thus, the increase of negative charge of BBST only plays a minor role in contributing to the decrease in work function under the same HC. Furthermore, it can be observed from Figure 12 that with increasing HC, the Li adsorption becomes increasingly more important than the charge effect in reducing the average work function. Hence, Li adsorption is the dominant factor for the reduction of work functions of Li_n/BBST systems, while the increases in negative charge and rumpling only play minor roles.

In Figure 13, the electrostatic potential distributions of BBST, **1(S)**, and **2a(D)** are shown with an isovalue of −0.12475 e/A³. As observed, an extra electrostatic field, induced by the apparent molecular dipole (Li⁺−B⁻), can be formed on BBST.[73,76] The direction of the extra electrostatic field is in favor of the escape of electrons, which has been well documented in previous studies of modifying work functions.[73,74] Therefore, we can draw a conclusion that the molecular dipole between Li and BBST generated by Li adsorption plays an important role in engineering the work function of BBST.

■ CONCLUSIONS

In summary, the geometries, binding energies, electronic structures and work functions of 14 structures of Li_n/BBST systems were investigated using first-principles density functional theory calculations. The minimum energy pathway simulation and thermodynamic analyses indicate that the clustering effect of Li adatoms on BBST is suppressed, and the computational results of binding energies demonstrate that the binding of Li adatoms to BBST is thermodynamically
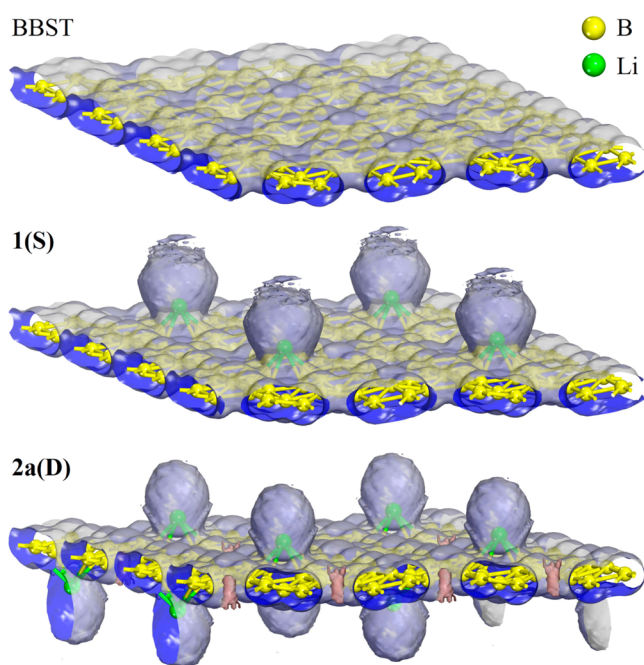
Figure 13. Distributions of electrostatic potentials for BBST, **1(S)**, and **2a(D)** systems.

favorable. Based on electronic structure and electron density analyses, we observed that electron transfer is from Li atoms and remote boron atoms to neighboring boron atoms, which is universal in the investigated Li_n/BBST systems. In addition, the bonding interaction between Li adatoms and the BBST substrate results from the strong hybridization between B $2p$ and Li $2p$ orbitals. Moreover, the work function of BBST can be effectively reduced by 11.8−44.5% by Li adsorption, which is dominantly due to the molecular dipole formed between Li and BBST. Indeed, the Fermi level plays a crucial role in determining the work functions of Li-adsorbed BBST systems, while the vacuum energy level has only a very slight impact. Importantly, the work functions of the investigated Li_n/BBST systems are lower than that of Mg, and some are even lower than that of Ca. Therefore, the Li-absorbed BBST materials could be promising candidates for electrode materials in electric devices.

■ ASSOCIATED CONTENT

Ⓢ Supporting Information

Simple discussion regarding "homogeneity degree of adsorption"; schematic diagrams of Li-shift pathways on BBST for Li/BBST system; rumplings (R) and average rumplings ($\overline{R}$) of Li_n/BBST systems; binding energies of Li_n/BBST systems as a function of HDA, where each polyline corresponds to the systems with the same HC; the optimized models, binding energies (E_b), and Li−C average bond lengths (L) of Li_n/graphene systems; slice of potential for Li_n/BBST systems, where gray and purple spheres represent boron and lithium atoms, respectively, and the three yellow spheres correspond to the boron atoms which are used to determine every slice of the electrostatic potential maps for the BBST, **1(S)**, **3a(D)**, and **5b(D)** systems; table of calculated binding energies (E_b) of Li_n/BBST, relative torsion energies of BBST substrates (ΔE_{BBST}), and cohesive energies (E_{coh}) of Li atoms. This material is available free of charge via the Internet at http://pubs.acs.org.

19698

dx.doi.org/10.1021/am504674p | *ACS Appl. Mater. Interfaces* 2014, 6, 19690−19701

■ AUTHOR INFORMATION

Corresponding Authors
*E-mail: yuhaitao@hlju.edu.cn.
*E-mail: chyflian@hlju.edu.cn.

Author Contributions
The paper was written through contributions of all authors. All authors have given approval to the final version of the paper.

Notes
The authors declare no competing financial interest.

■ ABBREVIATIONS

0D = zero-dimensional
1D = one-dimensional
2D = two-dimensional
CNT = carbon nanotube
BNT = boron nanotube
FE = field emission
AdNDP = Adaptive Natural Density Partitioning
SWBNT = single-walled boron nanotube
MWBNT = multiwalled boron nanotube
LED = light emitting diode
OLED = organic light emitting diode
OSC = organic solar cell
DFT = density functional theory
PW91 = Perdew−Wang
GGA = generalized gradient approximation
DNP = double numerical plus polarized
BZ = Brillouin zone
DOS = density of state
LST/QST = linear/quadratic synchronous transit
NEB = nudged elastic band
MEP = minimum energy pathway
BBST = buckled boron α-sheet
PBST = plane boron α-sheet
MHS = middle hollow site
Li_n/BBST = buckled boron α-sheet absorbed with n Li adatoms
HC = hole coverage
TDOS = total density of state
PDOS = partial density of state
NB = neighboring boron
RB = remote boron
BBST′(-1) = buckled boron α-sheet with charge of -1 e
BBST′(-2) = buckled boron α-sheet with charge of -2 e

■ REFERENCES

(1) Zhu, S.-E.; Li, F.; Wang, G.-W. Mechanochemistry of Fullerenes and Related Materials. *Chem. Soc. Rev.* **2013**, *42*, 7535−7570.
(2) Wang, C.; Takei, K.; Takahashi, T.; Javey, A. Carbon Nanotube Electronics-Moving Forward. *Chem. Soc. Rev.* **2013**, *42*, 2592−2609.
(3) Novoselov, K. S.; Fal'ko, V. I.; Colombo, L.; Gellert, P. R.; Schwab, M. G.; Kim, K. A Roadmap for Graphene. *Nature* **2012**, *490*, 192−200.
(4) Novoselov, K. S.; Geim, A. K.; Morozov, S. V.; Jiang, D.; Katsnelson, M. I.; Grigorieva, I. V.; Dubonos, S. V.; Firsov, A. A. Two-Dimensional Gas of Massless Dirac Fermions in Graphene. *Nature* **2005**, *438*, 197−200.

(5) Ghoshal, T.; Senthamaraikannan, R.; Shaw, M. T.; Holmes, J. D.; Morris, M. A. Fabrication of Ordered, Large Scale, Horizontally-Aligned Si Nanowire Arrays Based on an In Situ Hard Mask Block Copolymer Approach. *Adv. Mater.* **2014**, *26*, 1207−1216.
(6) Martinson, A. B. F.; Elam, J. W.; Hupp, J. T.; Pellin, M. J. ZnO Nanotube Based Dye-Sensitized Solar Cells. *Nano Lett.* **2007**, *7*, 2183−2187.
(7) Kang, T.-S.; Smith, A. P.; Taylor, B. E.; Durstock, M. F. Fabrication of Highly-Ordered TiO_2 Nanotube Arrays and Their Use in Dye-Sensitized Solar Cells. *Nano Lett.* **2009**, *9*, 601−606.
(8) Penev, E. S.; Bhowmick, S.; Sadrzadeh, A.; Yakobson, B. I. Polymorphism of Two-Dimensional Boron. *Nano Lett.* **2012**, *12*, 2441−2445.
(9) Tang, H.; Ismail-Beigi, S. First-Principles Study of Boron Sheets and Nanotubes. *Phys. Rev. B* **2010**, *82*, 115412.
(10) Lau, K. C.; Pandey, R. Thermodynamic Stability of Novel Boron Sheet Configurations. *J. Phys. Chem. B* **2008**, *112*, 10217−10220.
(11) Lau, K. C.; Pandey, R. Stability and Electronic Properties of Atomistically-Engineered 2D Boron Sheets. *J. Phys. Chem. C* **2007**, *111*, 2906−2912.
(12) Wu, X.; Dai, J.; Zhao, Y.; Zhuo, Z.; Yang, J.; Zeng, X. C. Two-Dimensional Boron Monolayer Sheets. *ACS Nano* **2012**, *6*, 7443−7453.
(13) Bezugly, V.; Kunstmann, J.; Grundkötter-Stock, B.; Frauenheim, T.; Niehaus, T.; Cuniberti, G. Highly Conductive Boron Nanotubes: Transport Properties, Work Functions, and Structural Stabilities. *ACS Nano* **2011**, *5*, 4997−5005.
(14) Lu, H.; Mu, Y.; Bai, H.; Chen, Q.; Li, S.-D. Binary Nature of Monolayer Boron Sheets from Ab Initio Global Searches. *J. Chem. Phys.* **2013**, *138*, 024701.
(15) Amsler, M.; Botti, S.; Marques, M. A. L.; Goedecker, S. Conducting Boron Sheets Formed by the Reconstruction of the α-Boron (111) Surface. *Phys. Rev. Lett.* **2013**, *111*, 136101.
(16) Yu, X.; Li, L.; Xu, X.-W.; Tang, C.-C. Prediction of Two-Dimensional Boron Sheets by Particle Swarm Optimization Algorithm. *J. Phys. Chem. C* **2012**, *116*, 20075−20079.
(17) Liu, Y.; Penev, E. S.; Yakobson, B. I. Probing the Synthesis of Two-Dimensional Boron by First-Principles Computations. *Angew. Chem., Int. Ed.* **2013**, *52*, 3156−3159.
(18) Liu, H.; Gao, J.; Zhao, J. From Boron Cluster to Two-Dimensional Boron Sheet on Cu(111) Surface: Growth Mechanism and Hole Formation. *Sci. Rep.* **2013**, *3*, 3238.
(19) Galeev, T. R.; Chen, Q.; Guo, J.-C.; Bai, H.; Miao, C.-Q.; Lu, H.-G.; Sergeeva, A. P.; Li, S.-D.; Boldyrev, A. I. Deciphering the Mystery of Hexagon Holes in an All-Boron Graphene α-Sheet. *Phys. Chem. Chem. Phys.* **2011**, *13*, 11575−11578.
(20) Piazza, Z. A.; Hu, H.-S.; Li, W.-L.; Zhao, Y.-F.; Li, J.; Wang, L.-S. Planar Hexagonal B_{36} as a Potential Basis for Extended Single-Atom Layer Boron Sheets. *Nat. Commun.* **2014**, *5*, 3113.
(21) An, H.; Liu, C. S.; Zeng, Z.; Fan, C.; Ju, X. Li-Doped B_2C Graphene as Potential Hydrogen Storage Medium. *Appl. Phys. Lett.* **2011**, *98*, 173101.
(22) Golberg, D.; Bando, Y.; Huang, Y.; Terao, T.; Mitome, M.; Tang, C.; Zhi, C. Boron Nitride Nanotubes and Nanosheets. *ACS Nano* **2010**, *4*, 2979−2993.
(23) Raidongia, K.; Nag, A.; Hembram, K. P. S. S.; Waghmare, U. V.; Datta, R.; Rao, C. N. R. BCN: A Graphene Analogue with Remarkable Adsorptive Properties. *Chem.—Eur. J.* **2010**, *16*, 149−157.
(24) Jiao, L.; Zhang, L.; Wang, X.; Diankov, G.; Dai, H. Narrow Graphene Nanoribbons from Carbon Nanotubes. *Nature* **2009**, *458*, 877−880.
(25) Bekyarova, E.; Itkis, M. E.; Ramesh, P.; Berger, C.; Sprinkle, M.; de Heer, W. A.; Haddon, R. C. Chemical Modification of Epitaxial Graphene: Spontaneous Grafting of Aryl Groups. *J. Am. Chem. Soc.* **2009**, *131*, 1336−1337.
(26) Chigo Anota, E.; Escobedo-Morales, A.; Salazar Villanueva, M.; Vazquez-Cuchillo, O.; Rubio Rosas, E. On the Influence of Point Defects on the Structural and Electronic Properties of Graphene-Like

Sheets: A Molecular Simulation Study. *J. Mol. Model.* **2013**, *19*, 839−846.

(27) Hernandez Rosas, J. J.; Ramirez Gutierrez, R. E.; Escobedo-Morales, A.; Chigo Anota, E. First Principles Calculations of the Electronic and Chemical Properties of Graphene, Graphane, and Graphene Oxide. *J. Mol. Model.* **2011**, *17*, 1133−1139.

(28) Tian, J.; Cai, J.; Hui, C.; Zhang, C.; Bao, L.; Gao, M.; Shen, C.; Gao, H. Boron Nanowires for Flexible Electronics. *Appl. Phys. Lett.* **2008**, *93*, 122105.

(29) Liu, F.; Shen, C.; Su, Z.; Ding, X.; Deng, S.; Chen, J.; Xu, N.; Gao, H. Metal-Like Single Crystalline Boron Nanotubes: Synthesis and In Situ Study on Electric Transport and Field Emission Properties. *J. Mater. Chem.* **2010**, *20*, 2197−2205.

(30) An, H.; Liu, C.-S.; Zeng, Z. Radial Deformation-Induced High-Capacity Hydrogen Storage in Li-Coated Zigzag Boron Nanotubes. *Phys. Rev. B* **2011**, *83*, 115456.

(31) Li, M.; Li, Y.; Zhou, Z.; Shen, P.; Chen, Z. Ca-Coated Boron Fullerenes and Nanotubes as Superior Hydrogen Storage Materials. *Nano Lett.* **2009**, *9*, 1944−1948.

(32) Li, Y.; Zhou, G.; Li, J.; Gu, B.-L.; Duan, W. Alkali-Metal-Doped B_{80} as High-Capacity Hydrogen Storage Media. *J. Phys. Chem. C* **2008**, *112*, 19268−19271.

(33) Banerjee, S.; Periyasamy, G.; Pati, S. K. Possible Application of 2D-Boron Sheets as Anode Material in Lithium Ion Battery: A DFT and AIMD Study. *J. Mater. Chem. A* **2014**, *2*, 3856−3864.

(34) De, S.; Willand, A.; Amsler, M.; Pochet, P.; Genovese, L.; Goedecker, S. Energy Landscape of Fullerene Materials: A Comparison of Boron to Boron Nitride and Carbon. *Phys. Rev. Lett.* **2011**, *106*, 225502.

(35) Pochet, P.; Genovese, L.; De, S.; Goedecker, S.; Caliste, D.; Ghasemi, S. A.; Bao, K.; Deutsch, T. Low-Energy Boron Fullerenes: Role of Disorder and Potential Synthesis Pathways. *Phys. Rev. B* **2011**, *83*, 081403.

(36) Zhao, J.; Wang, L.; Li, F.; Chen, Z. B_{80} and Other Medium-Sized Boron Clusters: Core−Shell Structures, Not Hollow Cages. *J. Phys. Chem. A* **2010**, *114*, 9969−9972.

(37) Özdoğan, C.; Mukhopadhyay, S.; Hayami, W.; Güvenç, Z. B.; Pandey, R.; Boustani, I. The Unusually Stable B_{100} Fullerene, Structural Transitions in Boron Nanostructures, and a Comparative Study of α- and γ-Boron and Sheets. *J. Phys. Chem. C* **2010**, *114*, 4362−4375.

(38) Gonzalez Szwacki, N.; Sadrzadeh, A.; Yakobson, B. I. B_{80} Fullerene: An Ab Initio Prediction of Geometry, Stability, and Electronic Structure. *Phys. Rev. Lett.* **2007**, *98*, 166804.

(39) Ciuparu, D.; Klie, R. F.; Zhu, Y.; Pfefferle, L. Synthesis of Pure Boron Single-Wall Nanotubes. *J. Phys. Chem. B* **2004**, *108*, 3967−3969.

(40) Cao, L. M.; Zhang, Z.; Sun, L. L.; Gao, C. X.; He, M.; Wang, Y. Q.; Li, Y. C.; Zhang, X. Y.; Li, G.; Zhang, J.; Wang, W. K. Well-Aligned Boron Nanowire Arrays. *Adv. Mater.* **2001**, *13*, 1701−1704.

(41) Zhu, D.; Kisi, E. Synthesis and Characterization of Boron/Boron Oxide Nanorods. *J. Aust. Ceram. Soc.* **2009**, *45*, 49−53.

(42) Wang, Z.; Shimizu, Y.; Sasaki, T.; Kawaguchi, K.; Kimura, K.; Koshizaki, N. Catalyst-Free Fabrication of Single Crystalline Boron Nanobelts by Laser Ablation. *Chem. Phys. Lett.* **2003**, *368*, 663−667.

(43) Xu, T. T.; Zheng, J.-G.; Wu, N.; Nicholls, A. W.; Roth, J. R.; Dikin, D. A.; Ruoff, R. S. Crystalline Boron Nanoribbons: Synthesis and Characterization. *Nano Lett.* **2004**, *4*, 963−968.

(44) Kwon, K. C.; Choi, K. S.; Kim, B. J.; Lee, J. L.; Kim, S. Y. Work-Function Decrease of Graphene Sheet Using Alkali Metal Carbonates. *J. Phys. Chem. C* **2012**, *116*, 26586−26591.

(45) Kwon, K. C.; Choi, K. S.; Kim, S. Y. Increased Work Function in Few-Layer Graphene Sheets via Metal Chloride Doping. *Adv. Funct. Mater.* **2012**, *22*, 4724−4731.

(46) Kumar, P. V.; Bernardi, M.; Grossman, J. C. The Impact of Functionalization on the Stability, Work Function, and Photoluminescence of Reduced Graphene Oxide. *ACS Nano* **2013**, *7*, 1638−1645.

(47) Jiao, N.; He, C. Y.; Zhang, C. X.; Peng, X. Y.; Zhang, K. W.; Sun, L. Z. Modulation Effect of Hydrogen and Fluorine Decoration on the Surface Work Function of BN Sheets. *AIP Adv.* **2012**, *2*, 022125.

(48) He, C.; Yu, Z.; Sun, L. Z.; Zhong, J. X. Work Functions of Boron Nitride Nanoribbons: First-Principles Study. *J. Comput. Theor. Nanosci.* **2012**, *9*, 16−22.

(49) Xie, Y.; Yu, H.; Zhang, H.; Fu, H. Tuning the Band Gaps and Work Functions via Topology and Carbon Concentration: A First-Principles Investigation of $C_x(BN)_y$ Compounds. *Phys. Chem. Chem. Phys.* **2012**, *14*, 4391−4397.

(50) Yu, Y.-J.; Zhao, Y.; Ryu, S.; Brus, L. E.; Kim, K. S.; Kim, P. Tuning the Graphene Work Function by Electric Field Effect. *Nano Lett.* **2009**, *9*, 3430−3434.

(51) Wang, B.; Gunther, S.; Wintterlin, J.; Bocquet, M. L. Periodicity, Work Function, and Reactivity of Graphene on Ru(0001) from First Principles. *New J. Phys.* **2010**, *12*, 043041.

(52) Wang, Y.; Tong, S. W.; Xu, X. F.; Özyilmaz, B.; Loh, K. P. Interface Engineering of Layer-by-Layer Stacked Graphene Anodes for High-Performance Organic Solar Cells. *Adv. Mater.* **2011**, *23*, 1514−1518.

(53) Shin, H.-J.; Choi, W. M.; Choi, D.; Han, G. H.; Yoon, S.-M.; Park, H.-K.; Kim, S.-W.; Jin, Y. W.; Lee, S. Y.; Kim, J. M.; Choi, J.-Y.; Lee, Y. H. Control of Electronic Structure of Graphene by Various Dopants and Their Effects on a Nanogenerator. *J. Am. Chem. Soc.* **2010**, *132*, 15603−15609.

(54) Gonga, H. R.; Nishi, Y.; Cho, K. Effects of Strain and Interface on Work Function of a Nb−W Metal Gate System. *Appl. Phys. Lett.* **2007**, *91*, 242105.

(55) Bae, G.; Cha, J.; Lee, H.; Park, W.; Park, N. Effects of Defects and Non-Coordinating Molecular Overlayers on the Work Function of Graphene and Energy-Level Alignment with Organic Molecules. *Carbon* **2012**, *50*, 851−856.

(56) Giovannetti, G.; Khomyakov, P. A.; Brocks, G.; Karpan, V. M.; van den Brink, J.; Kelly, P. J. Doping Graphene with Metal Contacts. *Phys. Rev. Lett.* **2008**, *101*, 026803−026803.

(57) Jin, L.; Fu, H.-G.; Xie, Y.; Yu, H.-T. Field Emission Properties of Capped Carbon Nanotubes Doped by Alkali Metals: A Theoretical Investigation. *Chin. Phys. B* **2012**, *21*, 057901.

(58) Fan, X.; Zheng, W. T.; Kuo, J.-L. Adsorption and Diffusion of Li on Pristine and Defective Graphene. *ACS Appl. Mater. Interfaces* **2012**, *4*, 2432−2438.

(59) Er, S.; de Wijs, G. A.; Brocks, G. DFT Study of Planar Boron Sheets: A New Template for Hydrogen Storage. *J. Phys. Chem. C* **2009**, *113*, 18962−18967.

(60) Perdew, J. P.; Chevary, J. A.; Vosko, S. H.; Jackson, K. A.; Pederson, M. R.; Singh, D. J.; Fiolhais, C. Atoms, Molecules, Solids, and Surfaces: Applications of the Generalized Gradient Approximation for Exchange and Correlation. *Phys. Rev. B* **1992**, *46*, 6671−6687.

(61) Er, S.; de Wijs, G. A.; Brocks, G. Hydrogen Storage by Polylithiated Molecules and Nanostructures. *J. Phys. Chem. C* **2009**, *113*, 8997−9002.

(62) Henkelman, G.; J, H. Improved Tangent Estimate in the Nudged Elastic Band Method for Finding Minimum Energy Paths and Saddle Points. *J. Chem. Phys.* **2000**, *113*, 9978−9985.

(63) Olsen, R. A.; Kroes, G. J.; Henkelman, G.; Arnaldsson, A.; Jónsson, H. Comparison of Methods for Finding Saddle Points without Knowledge of the Final States. *J. Chem. Phys.* **2004**, *121*, 9776−9792.

(64) Delley, B. An All-Electron Numerical Method for Solving the Local Density Functional for Polyatomic Molecules. *J. Chem. Phys.* **1990**, *92*, 508−517.

(65) Wang, Y. S.; Wang, F.; Li, M.; Xu, B.; Sun, Q.; Jia, Y. Theoretical Prediction of Hydrogen Storage on Li Decorated Planar Boron Sheets. *Appl. Surf. Sci.* **2012**, *258*, 8874−8879.

(66) Koh, W.; Choi, J. I.; Donaher, K.; Lee, S. G.; Jang, S. S. Mechanism of Li Adsorption on Carbon Nanotube−Fullerene Hybrid System: A First-Principles Study. *ACS Appl. Mater. Interfaces* **2011**, *3*, 1186−1194.

(67) Habenicht, B.; Teng, D.; Semidey-Flecha, L.; Sholl, D.; Xu, Y. Adsorption and Diffusion of 4d and 5d Transition Metal Adatoms on Graphene/Ru(0001) and the Implications for Cluster Nucleation. *Top Catal* **2014**, *57*, 69−79.

(68) Fan, X.; Zheng, W. T.; Kuo, J.-L.; Singh, D. J. Adsorption of Single Li and the Formation of Small Li Clusters on Graphene for the Anode of Lithium-Ion Batteries. *ACS Appl. Mater. Interfaces* **2013**, *5*, 7793−7797.

(69) Hussain, T.; De Sarkar, A.; Ahuja, R. Strain Induced Lithium Functionalized Graphane as a High Capacity Hydrogen Storage Material. *Appl. Phys. Lett.* **2012**, *101*, 103907.

(70) Lee, E.; Persson, K. A. Li Absorption and Intercalation in Single Layer Graphene and Few Layer Graphene by First Principles. *Nano Lett.* **2012**, *12*, 4624−4628.

(71) Zhou, L.-J.; Hou, Z. F.; Wu, L.-M. First-Principles Study of Lithium Adsorption and Diffusion on Graphene with Point Defects. *J. Phys. Chem. C* **2012**, *116*, 21780−21787.

(72) Shan, B.; Cho, K. First Principles Study of Work Functions of Single Wall Carbon Nanotubes. *Phys. Rev. Lett.* **2005**, *94*, 236602.

(73) Hofmann, O. T.; Egger, D. A.; Zojer, E. Work-Function Modification beyond Pinning: When Do Molecular Dipoles Count? *Nano Lett.* **2010**, *10*, 4369−4374.

(74) Rusu, P. C.; Giovannetti, G.; Weijtens, C.; Coehoorn, R.; Brocks, G. Work Function Pinning at Metal−Organic Interfaces. *J. Phys. Chem. C* **2009**, *113*, 9974−9977.

(75) Crispin, X.; Geskin, V.; Crispin, A.; Cornil, J.; Lazzaroni, R.; Salaneck, W. R.; Bredas, J.-L. Characterization of the Interface Dipole at Organic/Metal Interfaces. *J. Am. Chem. Soc.* **2002**, *124*, 8131−8141.

(76) Fulton, C. C.; Lucovsky, G.; Nemanich, R. J. Process-Dependent Band Structure Changes of Transition-Metal (Ti,Zr,Hf) Oxides on Si (100). *Appl. Phys. Lett.* **2004**, *84*, 580−582.